THE JOURNAL OF PHYSICAL CHEMISTRY C
A JOURNAL OF THE AMERICAN CHEMICAL SOCIETY

pubs.acs.org/JPCC

Article

Revealing the Quasi-Periodic Crystallographic Structure of Self-Assembled $SnTiS_3$ Misfit Compound

Nitul S. Rajput,* Hionsuck Baik, Jin-You Lu, Srinivasa Reddy Tamalampudi, Raman Sankar, Amal Al Ghaferi, and Matteo Chiesa*

Cite This: *J. Phys. Chem. C* 2021, 125, 9956–9964

Read Online

ACCESS | Metrics & More | Article Recommendations | Supporting Information

ABSTRACT: Chemical vapor transport synthesis of $SnTiS_3$ yields a self-assembled heterostructure of two distinct constituent materials, the semiconductor SnS and the semimetal TiS_2. The misfit layer compound, although thermodynamically stable, is structurally complex, and precise understanding of the structure is necessary for designing nanoengineered heterojunction compound devices or for theoretical studies. In our work, we reveal the unique complexity of the quasi-periodic structure of this heterostructure by systematically investigating the misfit compound using a set of advanced electron microscopy techniques. X-ray and electron diffraction patterns along with high-resolution scanning/transmission electron microscopy images obtained from different crystallographic orientations resolve the complexity of the sublattice component layer structure and reveal the uniquely bonded alignment among interlayers and a quasi-periodic arrangement of the sublayers. Density functional theory calculations embedded with the extracted structural information provide quantitative insights into the formation of self-assembled heterojunction structures where the nonpolar van der Waals interaction is found to play a dominant role in the structural alignment over the polar interlayer interaction.

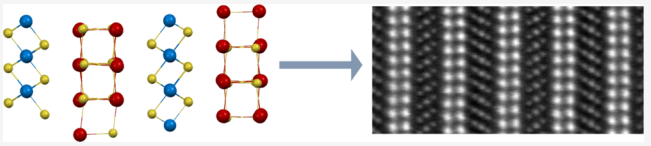

INTRODUCTION

Following the discovery of graphene, a huge interest propagated among the research community in isolating or growing new two-dimensional (2D) crystals. As a result, the 2D material family has grown with thousands of stable members.[1,2] Recently, fabricating 2D heterostructures consisting of different 2D layers has emerged as an active research area. Dean *et al.* demonstrated, for the first time, the design of a heterostructure for enhanced nanoelectronic applications where graphene was successfully stacked with an hBN 2D material.[3] Thereafter, many heterostructures have been developed and experimented on for their promise to fine-tune characteristics to suit specific applications in different areas.[4−8] These alternately stacked layers exhibit greater chemical stability than either of their component layers separately,[9] offering the opportunity to exploit the properties of their individual component materials.[10]

In these heterostructure materials, van der Waals forces are believed to play a dominant role in gluing the different layers together, but the full picture remains elusive.[11,12] It is true that the van der Waals interactions exist at the interface of the sublayers, which can be seen in a number of studies carried out using contact angle measurements and atomic force microscopy, and this nonpolar interaction could be the dominating factor that stabilizes the heterostructures.[10,13,14] On the other hand, the phenomenon of partial charge transfer (polar interaction) among the heterostructure sublattices is also speculated to be an important factor behind the stability of the compounds.[11,15,16] Particularly, for superconductivity in heterostructures, interface charge transfer and electron−phonon coupling have also been suggested as crucial interactions among their component layers.[17,18] Therefore, to understand the atomic-scale phenomenon of charge transfer and/or van der Waals interactions, a comprehensive study of the crystal structure and sublayer alignment is needed.

Alternating layers with dissimilar lattice symmetry give rise to a heterostructure with a less symmetric crystal structure, and thus they are mismatched. These are commonly referred to as misfit layer compounds. These misfit compounds can be made up of two or more crystal layers of different chemical compositions. One such family is transition-metal dichalcogenide misfit layer compounds $(MX)_nTX_2$ (M = Bi, Sn, Pb, or rare earths; X = S, Se; T = Ta, Ti, Nb, V; n = 1.08−1.28).[19] These misfit heterostructures have great promise in thermoelectric devices owing to their unique structural configurations, such as cross-plane sublattice mismatch, turbostratic disorder, and rotational disorder.[7,20] They also show other interesting properties such as superconductivity, unique topological behavior, and nonlinear optical properties, among

Received: December 1, 2020
Revised: April 16, 2021
Published: April 28, 2021

https://doi.org/10.1021/acs.jpcc.0c10756
J. Phys. Chem. C 2021, 125, 9956−9964

others.[17,21,22] These physical properties highly depend on the structural arrangement and the presence of structural defects/disorders. Atomic-scale electron microscopy imaging can derive a comprehensive information chart of the structure that could support to understand the observed physical properties and resolve the discrepancy between numerical prediction and experimental observations.

It is also observed that in most of the literature studies on misfit heterostructure materials, atomic-scale electron microscopy imaging is carried out only to validate the presence of the sublayers, and in-depth electron microscopic studies are for the most part absent.[17,23−25] However, in our experience, heterostructure materials are likely to possess various structural defects/disorders which could only be accessed through high-resolution scanning/transmission electron microscopy (S/TEM) imaging. Thus, a partial structural characterization could be misleading and can be the source of the discrepancy between numerical prediction and experimental observations.

Here, a systematic approach is employed, involving direct visualization using high-resolution S/TEM imaging to unveil the unique structural arrangement in the misfit compound—$SnTiS_3$. $SnTiS_3$ is an example of an interlayer complex compound composed of TiS_2 and SnS sublayers. The material is grown in a single-crystal form using a chemical vapor transport process. Thin lamellas are fabricated from the single-crystal $SnTiS_3$ to observe the structural disorder from different crystal orientations. The presence of high degree of sublattice mismatch along with stacking disorder, as evident by our high-resolution electron microscopy study, provides an insight about the unusual structure of the $SnTiS_3$ material, which reflects the generic nature of the structural arrangement of the misfit compound. Additionally, unique chevron-type alternating growth of TiS_2 (octahedral phase) in between the SnS sublayers is observed, which could be seen only along a particular orientation of the crystal. Further, we revert to density functional theory (DFT) calculation to analyze the heterojunction structures with different TiS_2 interlayer orientations that sheds light on how the van der Waals interaction plays a dominant role in the growth and stability of the misfit layer compounds. Our observations provide evidence to resolve the existing controversy regarding the dominating role of van der Waals interactions in misfit heterostructure materials.

MATERIALS AND METHODS

Bulk misfit single crystals of $SnTiS_3$ were grown using a chemical vapor transport (CVT) method, with chlorine as the transport agent, which is a cost-effective and efficient vapor transport to achieve the supersaturation of the expected final product. First, the powder of Sn, Ti, and S was weighted and thoroughly ground according to the ratio of Sn/Ti/S = 1:1:3.1. The powder mixture was then pressed into pellets and sealed under vacuum in a quartz tube and was heated at 650 °C for 4 days.

Then, the pre-reacted $SnTiS_3$ powder product was ground again and sealed with a variable amount of $TeCl_4$ (purity 4N) (100 mg) into an evacuated quartz tube with the diameter of 20 mm and length of 350 mm. The quartz tube was placed into a three-zone furnace with the temperature gradient of 900−800 °C for 2 weeks, and the powder mixture was placed in the hot end of the tube. The process parameters were optimized to grow single crystals of the misfit compound.[26] The single crystals were found in the middle and the hot end of the tube and were washed with ethanol to remove chlorine at the surface. The misfit single crystals have the typical dimensions of about $0.3 \times 3 \times 0.27$ mm^3.

A powder sample was prepared from the grown single crystal $SnTiS_3$ for the X-ray diffraction (XRD) experiment to provide information on the crystal unit cell dimensions and identify different crystallographic phases. The XRD experiment was done using a PANalytical Empyrean X-ray diffractometer with a Cu source (λ = 1.54056 Å).

In order to perform S/TEM investigation, thin lamellas from the single-crystal $SnTiS_3$ sample were prepared using a standard *in situ* lift-out procedure.[27] A dual-beam-focused ion beam system (Thermo Fisher Scientific, Helios 650) was used to fabricate the lamellas. The microscope is equipped with an advanced field emission SEM system with an Elstar column for high-resolution imaging and a Tomahawk Ga ion column for precise milling. For the fabrication of the lamella, a capping layer of Pt was deposited using the available precursor gas $(CH_3)_3Pt(CpCH_3)$. This additional layer protects the top surface layers from unnecessary erosion due to ion beam irradiation. A number of lamellas were prepared from the grown single crystal to observe the plane view and the cross-sectional view (from different orientations) of the sample. The experimental conditions for the preparation of the lamellas were kept unchanged for all of the specimens considered in this study. The lamellas were thinned down to the extent that a few holes appeared due to the ion-beam-milling process. The thickness over the prepared region of ∼4 μm (width) × 3 μm (height) was not uniform, and our investigation was performed at the thinnest crystalline regions in the proximity of the ion-beam-made holes.

For S/TEM imaging and electron diffraction measurement of the prepared lamellas, two different S/TEM microscopes were used. The first one is an image-corrected TEM system (Thermo Fisher Scientific, Titan G2), which was mostly used for preliminary investigation and electron diffraction experiment, and the other one is a double Cs-corrected Titan3 G2 60-300 S/TEM instrument (Thermo Fisher Scientific), which was mainly used for obtaining atomic-scale image and elemental mapping. α (A) and β (B) tilt ranges for the side entry double-tilt holders are ±40 and ±30°, respectively. For a side entry double-tilt holder in S/TEM, as the case in our S/TEM configurations, the difference in the tilt angle was calculated using the equation described by Kelly *et al.*[28]

All the measurements for S/TEM imaging and electron beam diffraction are obtained at 300 kV. The microscopes are equipped with a high-angle annular dark field (HAADF) detector along with other analytical techniques such as electron energy loss spectroscopy and energy-dispersive spectroscopy (EDS). Additionally, the integrated differential phase contrast (DPC) technique was used to image the samples with a certain zone axis. An integrated ring-shaped four-quadrant (4Q) detector was used to implement the DPC technique. The DPC images were formed by subtraction of the images of the opposite quadrants of the 4Q detector.

Successively, a multislice STEM simulation program (Dr. Probe) was used to simulate the HAADF image.[29] The simulations were performed using a 300 kV Gaussian electron beam with full width at half-maximum of 0.04 nm. During the simulation, twofold astigmatism aberration was considered. Frozen lattice configurations were 5 variants per slice. For the HAADF detector, the angular range was kept 40−180 mrad and the azimuth range was −5 to 5°.

https://doi.org/10.1021/acs.jpcc.0c10756
J. Phys. Chem. C 2021, 125, 9956−9964

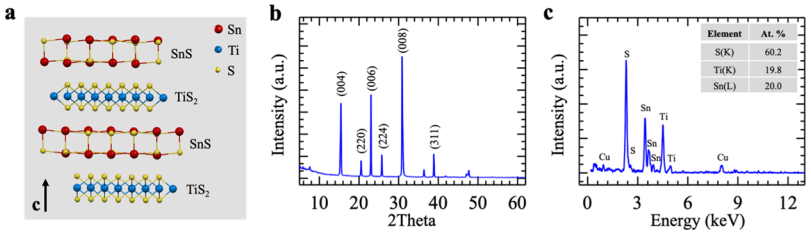

Figure 1. (a) Cross-sectional schematic view of the model structure. $SnTiS_3$ misfit compound: an alternate mixing of TiS_2 and SnS layers. (b) Powder XRD pattern with closely indexed planes. (c) EDS spectrum obtained from a thin slice of the material. Stoichiometric values shown in the inset indicate the atomic composition as Sn/Ti/S ≈ 1:1:3.

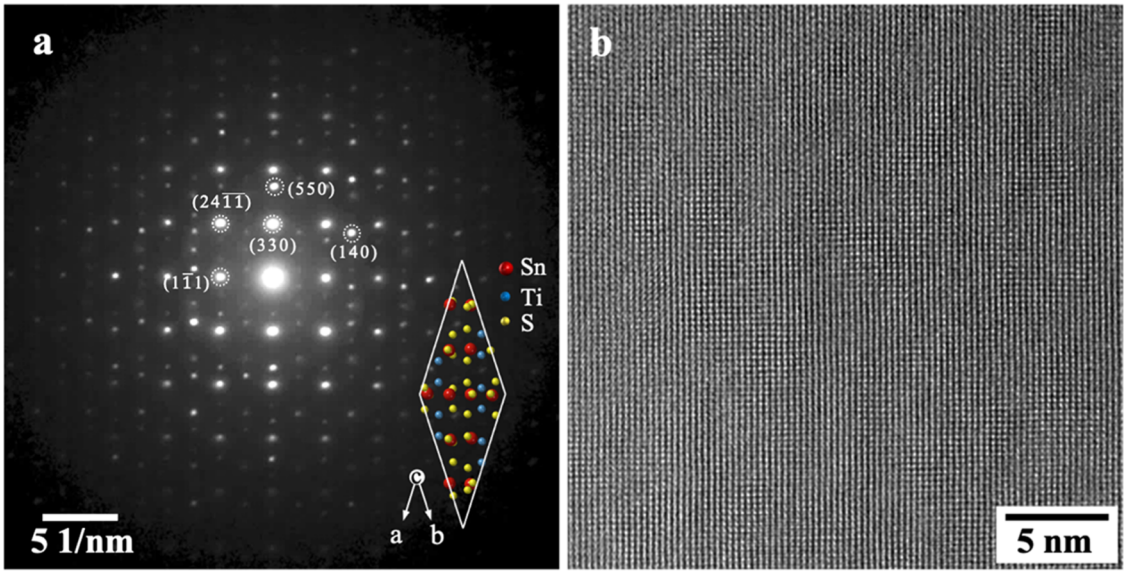

Figure 2. (a) Diffraction pattern obtained from the plan-view sample [001]. The inset indicates the orientation of the unit cell structure with respect to the obtained diffracted pattern. (b) Bright-field HR-TEM image obtained from the same orientation (top view of the crystal).

Plane-wave DFT simulations were performed using the Quantum ESPRESSO package 6-5 version.[30] The Perdew–Burke–Ernzerhof functional in generalized gradient approximations was used for the exchange–correlation energy with the ultrasoft pseudopotentials.[31] For van der Waals corrections, the DFT-D3 method of Grimme was applied in the total energy and geometry optimization calculations.[32] The kinetic energy cutoff and density cutoff were set as 100 and 800, respectively. For Monkhorst-Pack *k*-point setting, the 4 × 4 × 2 mesh was applied for $SnTiS_3$ bulk simulation, and the 2 × 2 × 1 mesh was applied for surface calculation. The criterion for the geometry optimization is satisfied once the total energy is less than 10^{-5} Ry and the interatomic force is less than 10^{-2} Ry/Bohr.

RESULTS AND DISCUSSION

A projected structure of the grown material is shown in Figure 1a. An animated 3D view of the structure is provided in the Supporting Information. The periodic structure has alternating layers of TiS_2 and SnS sublayers bonded with van der Waals forces. SnS carries two atomic layers that are sandwiched between TiS_2 layers.

A powder XRD pattern collected from the prepared sample is shown in Figure 1b. The sample provides various strong peaks with different intensities. The first intense peak appearing at ∼15.5° is indexed as the (004) plane. This provides a *d* (interplanar spacing) value of 5.72 Å. This conveys an estimated periodicity of the structure as 22.88 Å. Other planes in the XRD spectrum are closely indexed with respect to the closely related monoclinic system, however, without incorporating any stacking disorder.

The EDS spectrum collected from a thin slice of the material indicates the presence of the three elements. The estimated atomic % of the elements are shown in the inset. An approximate stoichiometry of the elements is found as Sn/Ti/S ≈ 1:1:3.

An electron diffraction pattern collected from a plan-view sample is shown in Figure 2a. A large number of reflections exist, indicating the presence of a variety of spatial frequencies which also shows the complex arrangement of the atoms in the misfit compound. Major spots are indexed in the diffraction image. The real space periodicities derived from the indexed planes are: (330): 0.28 nm, (550): 0.17 nm, (42$\bar{1}\bar{1}$): 0.20 nm, (140): 0.17 nm, and (1$\bar{1}$1): 0.29 nm. The real space orientation of the crystal structure is shown in the inset image. A high-resolution TEM image (plan view) is shown in Figure 2b. The electron diffraction pattern that is collected along the *c*-axis implies that the angle $\alpha = \beta \sim 90°$. On the other hand, the angle γ is evaluated through a set of measurements. Cross-sectional TEM lamellas are prepared in such a way to view along the [110] direction or close to this zone axis in S/TEM. Subsequently, the sample is tilted [by changing the α (A) and β (B) values] to orient along the [100] and [010] directions.

https://doi.org/10.1021/acs.jpcc.0c10756
J. Phys. Chem. C 2021, 125, 9956−9964

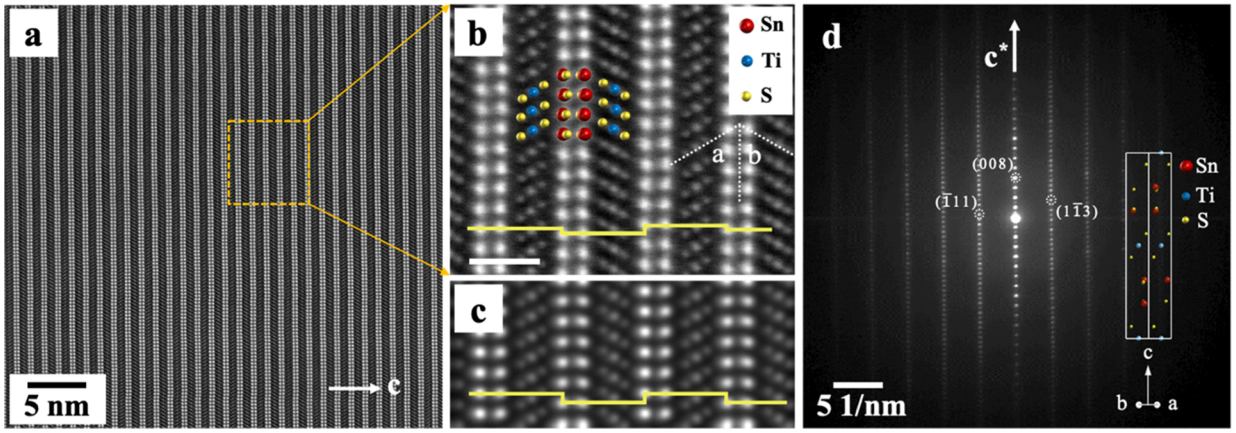

Figure 3. (a) High-resolution STEM image obtained from the zone axis [110]; (b) atomically resolved STEM image showing the layers as well as their specific positions; scale bar: 1 nm. (c) Simulated STEM image for comparison. (d) Electron diffraction pattern; the orientation of the unit cell structure is provided in the inset.

An average value of 35.5° is estimated using the procedure described above. This is the γ value made by the unit cell axes a and b. Keeping the c value and α, β, and γ values as estimated above, and assuming the crystal as a monoclinic system, values of $a = b$ are estimated as 9.08 Å. With the available parameters, a structure file is made in order to perform S/TEM and DFT simulation. This new crystal structure is in agreement with the trigonal phase of TiS_2 having $a = b = 3.417$ Å and $c = 5.823$ Å; $\alpha = \beta = 90.00°$ and $\gamma = 120.00°$ and with the orthorhombic phase of SnS having $a = 4.024$ Å, $b = 4.443$ Å, and $c = 11.68$ Å; $\alpha = \beta = \gamma = 90.00°$, respectively. It should be noted that the c value of the SnS crystal is nearly twice the value of the c parameter of TiS_2. This is believed to drive the growth of (001) planes of TiS_2 on top of the (001) plane of the orthorhombic SnS to ultimately initiate the growth of the 2D misfit $SnTiS_3$ crystal. Additionally, due to different unit cell parameters in the sublattice systems, the grown sublayers in the $SnTiS_3$ misfit compound will be strained, confirming the observations in other misfit crystallographic systems.[17]

A cross-sectional view of the sample prepared along [110] is shown in Figure 3a. The periodic structure of the material, that is, TiS_2 and SnS sublattices, can be clearly observed in the HAADF image. Two distinct layers with different atomic configurations can be noticed in the image where SnS layers appear relatively brighter than the TiS_2 layers. High-resolution EDS mapping taken over a scale of few microns indicates the sublayers (Supporting Information, Figure S1). The periodicity, as calculated from the image, is 2.37 nm, which is close to the value (22.88 Å) extracted from the XRD study. The STEM image obtained at a relatively higher magnification is shown in Figure 3b. The atomically resolved image clearly indicates the different atomic columns. The three atoms S, Ti, and S in the TiS_2 layers are in line, carrying the signature of the [110] orientation of 1T polymorph of TiS_2 (Supporting Information, Figure S2). It is interesting to note that the TiS_2 layers which seem to incline with respect to the SnS layers at a particular angle change the alignment alternately as the structures grow. This also implies that even though the intergrowths are structurally different, the layers are not completely independent from each other.

It is noticed that the angle made by one TiS_2 layer ($\angle a$, Figure 3b) with the SnS layer and the angle made by the neighboring TiS_2 layer ($\angle b$, Figure 3b) with the SnS layer are different, and in the present scenario, careful measurement indicates that $\angle a$ (~57°) is slightly lower than $\angle b$ (~60°), making up the total angle ($\angle a + \angle b$) ~ 117°. Additionally, the visibility of the atoms in the TiS_2 sublattices is found to be not uniform; the atomic columns are clearly resolved in the layer relating to $\angle a$, but they appear more streaked in the layer relating to $\angle b$. The structure file, which was created using the 1T phase of TiS_2, uses a regular stacking of TiS_2 layers. However, as we have observed the existence of chevron-type stacking of the TiS_2 layers with respect to the SnS layers in the STEM images, alternate TiS_2 layers are accordingly changed in the unit cell structure. Successively, the multislice STEM simulation was carried out to simulate the HAADF image using the reconstructed structure file. Figure 3c is a simulated STEM image along the [110] orientation. It should be noted that in the configured structure file, only the alternate TiS_2 layers are changed (flipped) in the unit cell structure, keeping $\angle a = \angle b$. Hence, the subtle streaking effect in the TiS_2 atomic columns in the layer relating to $\angle b$, as observed in the experimental image, does not appear in the simulated image. It is observed that there is a lateral displacement in the SnS sublattices, as marked by the yellow lines in Figure 3b,c. However, the lateral displacement in the experimental image is rather different from that of the simulated image (model structure) and does not appear to display any periodic pattern. In the model structure, the position of the SnS sublattices deviates by 0.14 nm (constant, shown by the yellow line); on the other hand, in the experimental image (Figure 3b), the position of the SnS sublattices varies irregularly (Supporting Information, Figure S3). This kind of stacking disorder, also observed in other misfit layer compounds, could be a unique structural property in misfit compounds.[33] These structural disorders disrupt phonon propagation along the cross-plane and result in low thermal conductivity, which is a desirable parameter for thermoelectric applications. Figure 3d shows the corresponding electron diffraction pattern. The orientation of the crystal in direct lattice space for the observed pattern is shown in the inset. The major spots are indexed and shown in the image. The extracted real space periodicities from the indexed planes are: (008): 0.29 nm, ($\bar{1}$10): 0.29 nm, and (1$\bar{1}$3): 0.26 nm.

Orientation of [1-10] of the structure is exactly perpendicular to [110]. To prepare a S/TEM specimen for observation along the [1-10] orientation, a lamella is prepared by rotating the sample by 90° with respect to the previous position. An

https://doi.org/10.1021/acs.jpcc.0c10756
J. Phys. Chem. C 2021, 125, 9956−9964

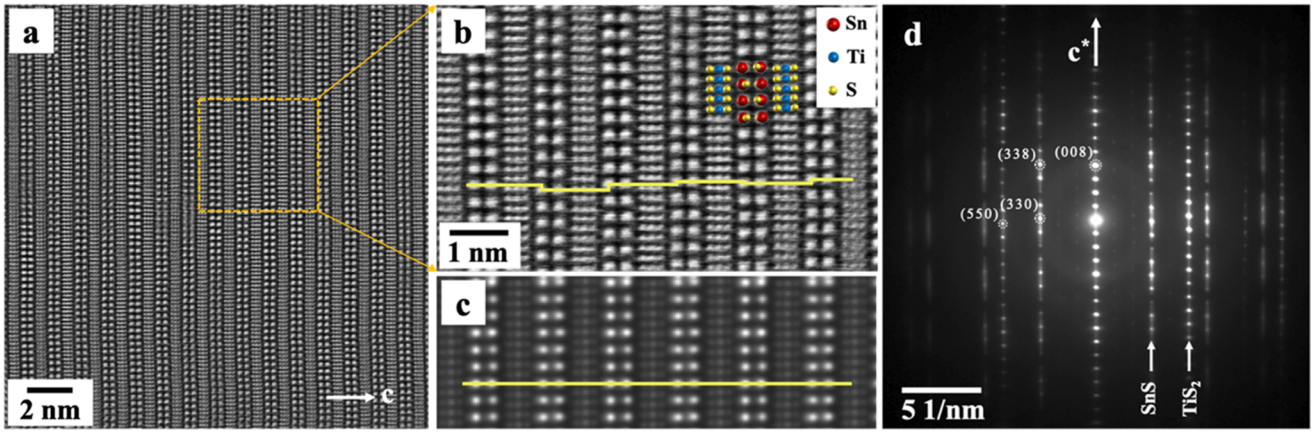

Figure 4. (a) High-resolution dDPC image obtained from the zone axis [1-10]. (b) Zoomed-in view of (a). (c) STEM simulation obtained using the structure file for comparison with the experimental image (b). (d) Electron diffraction pattern obtained from this orientation.

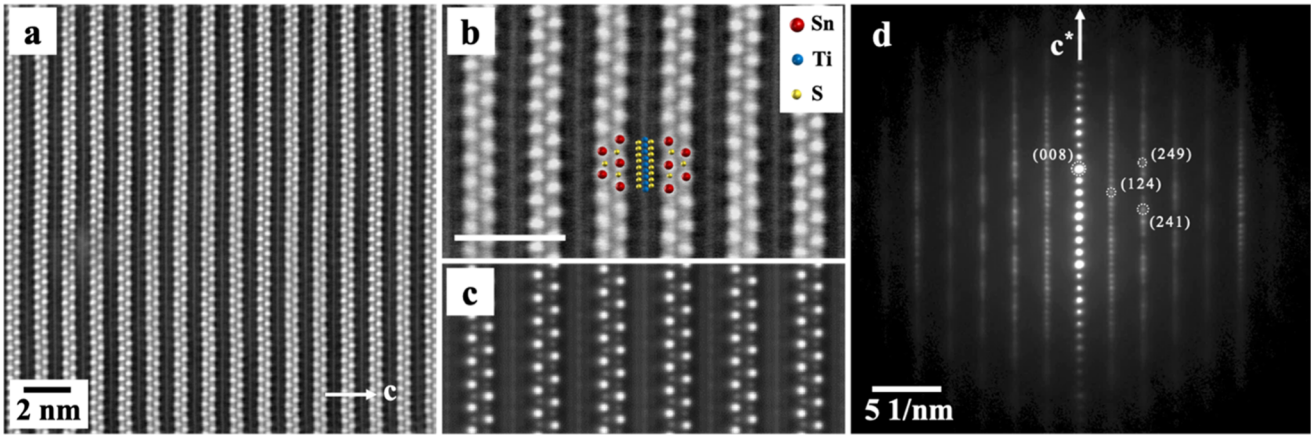

Figure 5. (a) High-resolution diffraction phase contrast image (STEM) obtained from the zone axis [-210]. (b) High-magnification view from (a); scale bar = 2 nm; (c) STEM simulation image obtained using the structure file. (d) Electron diffraction pattern.

inverted differentiated DPC (dDPC) image collected from this orientation is shown in Figure 4a. It is noticed that the S atoms can be better resolved with the Ti atoms in the TiS_2 layer with the help of the dDPC technique. The STEM image also corresponds to the projected sketch, as shown in Figure 1a. The dDPC image reflects the periodic patterns of SnS and TiS_2 without any defect or vacancy. However, a close look reveals that some amount of undulation is present in the periodic structure. The observed "undulation" or "rumpling" in the images is likely an experimental artifact due to the environmental instability. Long periodic undulation, as observed in other heterostructures,[33] is indeed found to be absent in this crystal. A high-magnification image is shown in Figure 4b. For comparison with the model structure, a simulated STEM (HAADF) image is shown in Figure 4c. A noticeable intensity difference between the sublayers is observed in Figure 4c, as compared to the experimental image 4b, which is because the simulated image 4c was acquired using a standard HAADF detector. As we can see, the model structure is free of any stacking disorder in the SnS sublattice system (represented by the yellow line in Figure 4c). In comparison, the actual structure contains some amount of stacking disorder in the SnS sublattice. This is shown by the yellow zigzag line in Figure 4b. The disorder in the stacking of the sublattices is observed to be random and does not follow any specific pattern, which implies that the nature of the stacking disorder cannot be introduced in the model structure to create a more realistic unit cell structure. A diffraction pattern obtained from this orientation is shown in Figure 4d. Individual reflections due to SnS and TiS_2 layers appear separately in the electron diffraction pattern which is due to the mismatch in their basis lattice vectors, also known as incommensurability.[34] The observed streaking of the SnS reflections in the electron diffraction pattern is because of the stacking disorder of the SnS sublattice system, as noted in Figure 4b. A simulated electron diffraction pattern (300 keV, camera constant = 19.69 Å mm) is shown in Figure S4 (Supporting Information). The observed weak spots can be seen in the experimental image as well (Figure 4d). However, as the stacking disorder is not included in the structure file, the corresponding outcome (due to stacking disorder), the streaking in the SnS reflections, is not observed in the simulated image (Figure S4).

Major spots in the diffraction pattern are indexed. The indexed (008) plane gives the real lattice spacing value of 0.29 nm. Other indexed planes provide real space periodicities of (330): 0.28 nm, (550): 0.17 nm, and (338): 0.20 nm.

The incommensurability nature between the TiS_2 and SnS sublattices is observed from other crystalline orientations as well. As an example, STEM images collected from the zone axis [-210] are shown in Figure 5. Zone axis [-210] makes an angle of ∼46° with [-110] and ∼44° with [-1-10]. The visibility of the TiS_2 layers is much lower than the

https://doi.org/10.1021/acs.jpcc.0c10756
J. Phys. Chem. C 2021, 125, 9956−9964

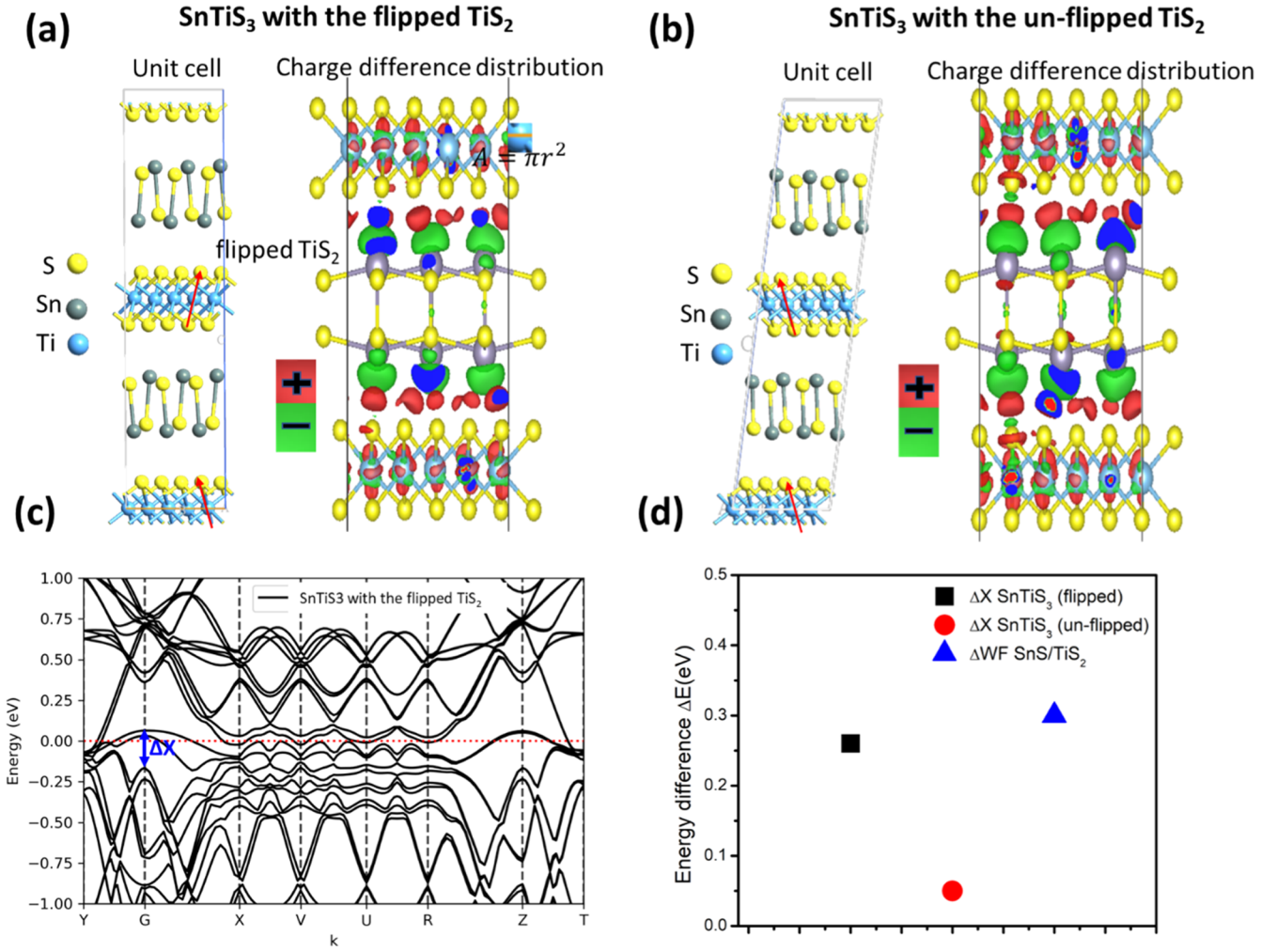

Figure 6. Unit cell and charge density difference distributions of the DFT-calculated $SnTiS_3$ misfit compound with flipped (a) and unflipped (b) TiS_2 layers. In the charge density difference distribution, the charge gain and charge loss regions are shown in red and blue colors, respectively. (c) DFT-calculated electronic band structures of the $SnTiS_3$ misfit compound with flipped layers. (d) Relative energy difference in the band diagram, where ΔX is the relative energy difference denoted in Figure 6c and ΔWF is the work function difference between individual SnS and TiS_2 monolayers.

Table 1. Summary of DFT-Relaxed Structures of the $SnTiS_3$ Misfit Compound with Flipped and Unflipped TiS_2 Layers

materials	crystal	a (Å)	b (Å)	c (Å)	α (deg)	β (deg)	γ (deg)
EXP-$SnTiS_3$	monoclinic[a]	9.08	9.08	22.88	~90	~90	35.5
DFT-$SnTiS_3$ (flipped TiS_2)	triclinic	9.02	9.02	23.31	89.07	89.07	37.59
DFT-$SnTiS_3$ (unflipped TiS_2)	triclinic	9.03	9.03	23.36	87.61	92.39	37.59

[a]Assuming $\alpha = \beta = 90°$.

corresponding SnS layers. However, an intensity profile taken along the c-axis clearly indicates the presence of the layers (Supporting Information, Figure S5). A high-magnification image is shown in Figure 5b. A simulated STEM image obtained from the structure file for comparison is shown in Figure 5c. A closer look indicates that a smooth periodic variation of the SnS sublattices is missing in the experimental image (Figure 5b), as compared to the simulated image (Figure 5c). This is similar to the observations made in other zone axes (Figures 3 and 4). The corresponding diffraction pattern collected along this zone axis is shown in Figure 5d. Some of the major spots are indexed in the diffraction image. The indexed plane (008) provides the real space periodicity of 0.29 nm. The derived real space values corresponding to other indexed planes are as follows: (124): 0.34 nm, (249): 0.16 nm, and (241): 0.21 nm.

To theoretically investigate the structures of $SnTiS_3$ in terms of energy perspective, we have chosen two different types of structures of $SnTiS_3$: one has a flipped TiS_2 layer (as observed in Figure 3), and the other one has a regular (unflipped) TiS_2 layer (Figure 6a,b). In order to ensure the configuration reaching the overall minimum energy state, the structures of initial configurations are optimized by performing DFT geometry optimization. The simulation results show that both optimized crystal structures belong to the triclinic crystal with similar lattice constants but with a noticeable difference in their α and β, as summarized in Table 1. First, we consider these two structures in their bulk form, which has 52 atoms per

https://doi.org/10.1021/acs.jpcc.0c10756
J. Phys. Chem. C 2021, 125, 9956−9964

unit cell. The DFT-calculated energy difference $\triangle U$ of these two optimized bulk $SnTiS_3$ systems is -2.4×10^{-3} eV per unit cell, as given by eq 1, which has the same order as that of DFT-D3 energy resolution.

$$\Delta U|_{\text{unit\_cell}} = E_{\text{flipped}} - E_{\text{un-flipped}} \quad (1)$$

where E is the total energy of the system. As it comes to layer system, which consists of three component layers (2L for TiS_2; 1L for SnS; total 42 atoms), the energy difference between these two structures in the layer form is calculated as -1.04×10^{-1} eV/unit cell. Investigations on both bulk and layered $SnTiS_3$ show that the structures with the flipped TiS_2 layer have lower formation (cohesive) energy (more negative), indicating a more thermodynamically stable structure. In addition, it should be noted that the energy difference is more pronounced for layered $SnTiS_3$ structures.

To give insights into the interlayered binding among the component layers of $SnTiS_3$, we have also investigated their charge density difference distributions, as given by eq 2[35]

$$\Delta\rho = \rho_{\text{tot}} - \rho_{\text{Sns}} - \rho_{\text{TiS}_2} \quad (2)$$

where ρ is the electron charge density in units of 0.01 e/(Å^3). The charge density difference distributions of the two types of layered $SnTiS_3$ structures show that the polar binding between SnS and TiS_2 results from the Sn atom of SnS coupled with the S atoms of TiS_2, where the charge gain and charge loss regions resulting from the component layer interaction are shown in red and blue colors, respectively. Besides, the nonpolar van der Waals interactions, also called London dispersion forces, cannot be observed in the charge difference distribution due to their transient nature. Similar charge difference density distributions of these two structures in Figure 6a,b show a similar polar interaction among the component layers, although the structure with unflipped TiS_2 layers has a larger charge density difference (stronger polar interaction). In combination with our relative energy calculation, in eq 1, we can summarize that $SnTiS_3$ with flipped TiS_2 has slightly less polar interaction and much stronger van der Waals interaction, as compared to the one with unflipped TiS_2. Therefore, the van der Waals interaction is the dominant factor in determining the sublattice layer configuration during the growth process. The relative energy calculations also indicate that the van der Waals interaction is more pronounced for the layered structure by a factor of nearly 60 times. Moreover, we compare the electronic band structures of the SnTiS3 structures in their bulk form, as shown in Figure 6c,d. The calculated effective electronic band structure of $SnTiS_3$ retrieved from the TEM image is nearly a superposition of the semiconductor SnS and semimetal TiS_2 component layers, which agrees with the recently reported findings that metal-like $SnTiS_3$ thin flakes have a strong band gap emission at 1.9 eV.[26] The work function difference between the monolayer SnS (4.8 eV) and TiS_2 (5.1 eV) is 0.3 eV, which is close to the relative energy shift denoted as ΔX in Figure 6c. This agreement explains how the effective band structure of the $SnTiS_3$ crystal structure is superpositioned by the individual band structures of the component layers. Moreover, when it comes to $SnTiS_3$ with the unflipped component TiS_2, the energy shift ΔX is 0.05 eV, and such a small difference results from a higher charge transfer between component layers. Owing to the weak van der Waals interaction within the misfit layer stackings, the properties of the superpositioned electronic band structures of $SnTiS_3$ do not significantly change with different structures; however, we can still observe that the alignment between the two electronic band structures of the SnS and TiS_2 component layers is changed with the sublattice TiS_2 structures.

We also compare the DFT-relaxed $SnTiS_3$ layered structures with the flipped and unflipped TiS_2 layers. In Figure S6 of the Supporting Information, no corrugations between successive layers are observed, and this agrees with the TEM characterization. When it comes to in-plane relaxations, the SnS component layers in the two types of DFT-relaxed $SnTiS_3$ show a significant difference with each other, as indicated by Δd_1 and Δd_2 of Sn−S in Figure 7. Specifically, for $SnTiS_3$ with flipped TiS_2 layers, Δd_1 is larger than Δd_2 by 0.58 Å; however, for $SnTiS_3$ with unflipped TiS_2 layers, Δd_1 is nearly the same as Δd_2.

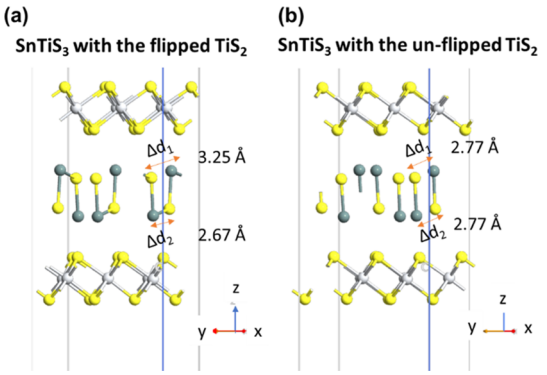

Figure 7. DFT-relaxed structures of the $SnTiS_3$ misfit compound with flipped (a) and unflipped (b) TiS_2 layers.

An alignment between these two component layers might be an exciting topic for future study, as $SnTiS_3$ is a promising candidate for thermoelectric applications. The figure of merit (efficiency) of a thermoelectric material is defined as $zT = \alpha^2\sigma T/\kappa$, where α is the Seebeck coefficient, σ is the electrical conductivity, $\alpha^2\sigma$ is termed as the power factor, T is the absolute temperature, and κ is the total thermal conductivity. In order to achieve high figure of merits, chemical structures should be designed in a way that phonon transport is inhibited, leading to a reduction in thermal conductivity without compromising electron mobility. TiS_2 has a high power factor; however, due to its high value of thermal conductivity, its figure of merit zT is low. However, this can be improved by intercalating with SnS layers, which act as a barrier to the phonon propagation, thus reducing the thermal conductivity. The presence of a high degree of sublattice mismatch along with stacking disorder, as evident by our high-resolution electron microscopy study, provides a clear hint about how $SnTiS_3$ might exhibit enhanced thermoelectric properties.[20,36] Additionally, the observed chevron-type alternating growth of TiS_2 (octahedral phase) in between the SnS sublayers, which is a unique configuration that could only be observed along a crystalline orientation, indicates the degree of complexity in the misfit compound crystal structure.

CONCLUSIONS

The structure of the misfit compound $SnTiS_3$ grown using the CVT process is systematically investigated using advanced electron microscopy and diffraction methods. Lamellas prepared along the different zone axes of the material and

https://doi.org/10.1021/acs.jpcc.0c10756
J. Phys. Chem. C 2021, 125, 9956−9964

subsequent imaging in S/TEM reveal interesting structural information about the material. The atomic resolution S/TEM images obtained from different crystal orientations show the presence of the sublattice layer structure and its stacking disorder throughout the material. The unique chevron-type growth of the 1T-TiS_2 sublayers with respect to the SnS layers in the heterostructure appears to be due to the lower formation energy of the structure, as manifested by the DFT study. DFT simulation results also show that the charge transfer does not change much with different component layer alignments, but the van der Waals force dominates during the growth of the misfit compound. The presence of structural complexity in $SnTiS_3$, as indicated by our study, indicates the likely presence of such complexity in other misfit materials as well, and a comprehensive study is essential to open potential applications in the creation of heterojunction devices.

■ ASSOCIATED CONTENT

Supporting Information

The Supporting Information is available free of charge at https://pubs.acs.org/doi/10.1021/acs.jpcc.0c10756.

EDS mapping, TiS_2 crystal structure in octahedral phase, stacking disorder, simulated electron diffraction image, intensity line profile [-210], and structural corrugations (PDF)

Crystal structure (AVI)

■ AUTHOR INFORMATION

Corresponding Authors

Nitul S. Rajput − *Laboratory for Energy and NanoScience (LENS), Khalifa University of Science and Technology, Abu Dhabi 54224, United Arab Emirates; Department of Mechanical and Materials Engineering, Khalifa University of Science and Technology, Abu Dhabi 54224, United Arab Emirates; Advanced Materials Research Center, Technology Innovation Institute, Abu Dhabi 9639, United Arab Emirates;* orcid.org/0000-0002-2516-7638; Email: nitul.rajput@am.tii.ae

Matteo Chiesa − *Laboratory for Energy and NanoScience (LENS), Khalifa University of Science and Technology, Abu Dhabi 54224, United Arab Emirates; Department of Mechanical and Materials Engineering, Khalifa University of Science and Technology, Abu Dhabi 54224, United Arab Emirates; Department of Physics and Technology, UiT The Arctic University of Norway, 9010 Tromsø, Norway;* Email: matteo.chiesa@ku.ac.ae

Authors

Hionsuck Baik − *Korea Basic Science Institute (KBSI), Seoul 02841, Korea;* orcid.org/0000-0002-5745-4404

Jin-You Lu − *Laboratory for Energy and NanoScience (LENS), Khalifa University of Science and Technology, Abu Dhabi 54224, United Arab Emirates; Department of Mechanical and Materials Engineering, Khalifa University of Science and Technology, Abu Dhabi 54224, United Arab Emirates; Advanced Materials Research Center, Technology Innovation Institute, Abu Dhabi 9639, United Arab Emirates*

Srinivasa Reddy Tamalampudi − *Laboratory for Energy and NanoScience (LENS), Khalifa University of Science and Technology, Abu Dhabi 54224, United Arab Emirates; Department of Mechanical and Materials Engineering, Khalifa University of Science and Technology, Abu Dhabi 54224, United Arab Emirates;* orcid.org/0000-0002-3922-0073

Raman Sankar − *Institute of Physics, Academia Sinica, Taipei 10617, Taiwan;* orcid.org/0000-0003-4702-2517

Amal Al Ghaferi − *Laboratory for Energy and NanoScience (LENS), Khalifa University of Science and Technology, Abu Dhabi 54224, United Arab Emirates; Department of Mechanical and Materials Engineering, Khalifa University of Science and Technology, Abu Dhabi 54224, United Arab Emirates*

Complete contact information is available at: https://pubs.acs.org/10.1021/acs.jpcc.0c10756

Notes

The authors declare no competing financial interest.

■ ACKNOWLEDGMENTS

This work was funded under the Cooperative Agreement between Khalifa University of Science and Technology, Masdar Campus, Abu Dhabi, UAE, and Massachusetts Institute of Technology (MIT), Cambridge, MA, USA, Reference Number FR2017-000001. We also acknowledge the support from the collaborative program between Khalifa University and Korea Basic Science Institute KU-KBSI (Project C040000). R.S. acknowledges financial support provided by the Ministry of Science and Technology in Taiwan under project number MOST-108-2112-M-001-049-MY2 and Academia Sinica for the budget of AS-iMATE-109-13.

■ REFERENCES

(1) Ashton, M.; Paul, J.; Sinnott, S. B.; Hennig, R. G. Topology-Scaling Identification of Layered Solids and Stable Exfoliated 2D Materials. *Phys. Rev. Lett.* **2017**, *118*, 106101.

(2) MaterialsWeb Databases of structural, electronic, and thermodynamic data for 2D/3D materials. https://2dmaterialsweb.org/, accessed Nov 29, 2020.

(3) Dean, C. R.; Young, A. F.; Meric, I.; Lee, C.; Wang, L.; Sorgenfrei, S.; Watanabe, K.; Taniguchi, T.; Kim, P.; Shepard, K. L.; et al. Boron nitride substrates for high-quality graphene electronics. *Nat. Nanotechnol.* **2010**, *5*, 722−726.

(4) Liang, S.-J.; Cheng, B.; Cui, X.; Miao, F. Van der Waals Heterostructures for High-Performance Device Applications: Challenges and Opportunities. *Adv. Mater.* **2020**, *32*, 1903800.

(5) Wang, H.; Liu, F.; Fu, W.; Fang, Z.; Zhou, W.; Liu, Z. Two-dimensional heterostructures: fabrication, characterization, and application. *Nanoscale* **2014**, *6*, 12250−12272.

(6) Li, C.; Zhou, P.; Zhang, D. W. Devices and applications of van der Waals heterostructures. *J. Semicond.* **2017**, *38*, 031005.

(7) Merrill, D.; Moore, D.; Bauers, S.; Falmbigl, M.; Johnson, D. Misfit Layer Compounds and Ferecrystals: Model Systems for Thermoelectric Nanocomposites. *Materials* **2015**, *8*, 2000−2029.

(8) Putri, Y. E.; Wan, C.; Zhang, R.; Mori, T.; Koumoto, K. Thermoelectric performance enhancement of (BiS)1.2(TiS2)2 misfit layer sulfide by chromium doping. *J. Adv. Ceram.* **2013**, *2*, 42−48.

(9) Fang, C. M.; Groot, R. A. d.; Wiegers, G. A.; Haas, C. Electronic structure of the misfit layer compound : band structure calculations and photoelectron spectra. *J. Phys.: Condens. Matter* **1996**, *8*, 1663−1676.

(10) Tamalampudi, S. R.; Santos, S.; Lai, C.-Y.; Olukan, T. A.; Lu, J.-Y.; Rajput, N.; Chiesa, M. Rapid discrimination of chemically distinctive surface terminations in 2D material based heterostructures by direct van der Waals identification. *Rev. Sci. Instrum.* **2020**, *91*, 023907.

(11) Ettema, A. R. H. F.; Haas, C. An X-ray photoemission spectroscopy study of interlayer charge transfer in some misfit layer compounds. *J. Phys.: Condens. Matter* **1993**, *5*, 3817−3826.
(12) Fang, C. M.; Ettema, A. R. H. F.; Haas, C.; Wiegers, G. A.; van Leuken, H.; de Groot, R. A. Electronic structure of the misfit-layer compound (SnS)1.17NbS2 deduced from band-structure calculations and photoelectron spectra. *Phys. Rev. B: Condens. Matter Mater. Phys.* **1995**, *52*, 2336−2347.
(13) Annamalai, M.; Gopinadhan, K.; Han, S. A.; Saha, S.; Park, H. J.; Cho, E. B.; Kumar, B.; Patra, A.; Kim, S.-W.; Venkatesan, T. Surface energy and wettability of van der Waals structures. *Nanoscale* **2016**, *8*, 5764−5770.
(14) Lu, J.-Y.; Lai, C.-Y.; Almansoori, I.; Chiesa, M. The evolution in graphitic surface wettability with first-principles quantum simulations: the counterintuitive role of water. *Phys. Chem. Chem. Phys.* **2018**, *20*, 22636−22644.
(15) Meerschaut, A.; Moëlo, Y.; Cario, L.; Lafond, A.; Deudon, C. Charge Transfer in Misfit Layer Chalcogenides, [(MX)n]1+x(TX2)-m: a Key for Understanding their Stability and Properties. *Mol. Cryst. Liq. Cryst. Sci. Technol., Sect. A* **2000**, *341*, 1−8.
(16) Cario, L.; Johrendt, D.; Lafond, A.; Felser, C.; Meerschaut, A.; Rouxel, J. Stability and charge transfer in the misfit compound $(LaS)(SrS)_{0.2}CrS_2$: Ab initio band-structure calculations. *Phys. Rev. B: Condens. Matter Mater. Phys.* **1997**, *55*, 9409−9414.
(17) Sankar, R.; Peramaiyan, G.; Panneer Muthuselvam, I.; Wen, C.-Y.; Xu, X.; Chou, F. C. Superconductivity in a Misfit Layered (SnS)1.15(TaS2) Compound. *Chem. Mater.* **2018**, *30*, 1373−1378.
(18) Zhang, H.; Zhang, D.; Lu, X.; Liu, C.; Zhou, G.; Ma, X.; Wang, L.; Jiang, P.; Xue, Q.-K.; Bao, X. Origin of charge transfer and enhanced electron−phonon coupling in single unit-cell FeSe films on SrTiO3. *Nat. Commun.* **2017**, *8*, 214.
(19) Rouxel, J.; Meerschaut, A.; Wiegers, G. A. Chalcogenide misfit layer compounds. *J. Alloys Compd.* **1995**, *229*, 144−157.
(20) Yin, C.; Hu, Q.; Tang, M.; Liu, H.; Chen, Z.; Wang, Z.; Ang, R. Boosting the thermoelectric performance of misfit-layered (SnS)1.2-(TiS2)2 by a Co- and Cu-substituted alloying effect. *J. Mater. Chem. A* **2018**, *6*, 22909−22914.
(21) Li, J.; Yang, K.; Du, L.; Yi, J.; Huang, J.; Zhang, J.; He, Y.; Huang, B.; Miao, L.; Zhao, C.; et al. Nonlinear Optical Response in Natural van der Waals Heterostructures. *Adv. Opt. Mater.* **2020**, *8*, 2000382.
(22) Wu, J.; Liu, F.; Sasase, M.; Ienaga, K.; Obata, Y.; Yukawa, R.; Horiba, K.; Kumigashira, H.; Okuma, S.; Inoshita, T.; et al. Natural van der Waals heterostructural single crystals with both magnetic and topological properties. *Sci. Adv.* **2019**, *5*, No. eaax9989.
(23) Atkins, R.; Wilson, J.; Zschack, P.; Grosse, C.; Neumann, W.; Johnson, D. C. Synthesis of [(SnSe)1.15]m(TaSe2)n Ferecrystals: Structurally Tunable Metallic Compounds. *Chem. Mater.* **2012**, *24*, 4594−4599.
(24) Giang, N.; Xu, Q.; Hor, Y. S.; Williams, A. J.; Dutton, S. E.; Zandbergen, H. W.; Cava, R. J. Superconductivity at 2.3 K in the misfit compound $(PbSe)_{1.16}$ $(TiSe_2)_2$. *Phys. Rev. B: Condens. Matter Mater. Phys.* **2010**, *82*, 024503.
(25) Wang, N. Z.; Yuan, S. F.; Cong, R.; Lu, X. F.; Meng, F. B.; Shang, C.; Chen, X. H. Structure and physical properties of the misfit compounds (PbSe) 1.16 (TiSe 2) m (m = 1, 2). *Europhys. Lett.* **2015**, *112*, 67007.
(26) Tamalampudi, S. R.; Lu, J.-Y.; Rajput, N.; Lai, C.-Y.; Alfakes, B.; Sankar, R.; Apostoleris, H.; Patole, P.; Almansouri, I.; Chiesa, M. Superposition of semiconductor and semi-metal properties of self-assembled 2D SnTiS3 heterostructures. *npj 2D Mater. Appl.* **2020**, *4*, 23.
(27) Schaffer, M.; Schaffer, B.; Ramasse, Q. Sample preparation for atomic-resolution STEM at low voltages by FIB. *Ultramicroscopy* **2012**, *114*, 62−71.
(28) Kelly, P. M.; Wauchope, C. J.; Zhang, X. Calculation of overall tilt angles for a double tilt holder in a TEM. *Microsc. Res. Tech.* **1994**, *28*, 448−451.
(29) Barthel, J. Dr. Probe: A software for high-resolution STEM image simulation. *Ultramicroscopy* **2018**, *193*, 1−11.
(30) Giannozzi, P.; Andreussi, O.; Brumme, T.; Bunau, O.; Buongiorno Nardelli, M.; Calandra, M.; Car, R.; Cavazzoni, C.; Ceresoli, D.; Cococcioni, M.; et al. Advanced capabilities for materials modelling with Quantum ESPRESSO. *J. Phys.: Condens. Matter* **2017**, *29*, 465901.
(31) Paier, J.; Hirschl, R.; Marsman, M.; Kresse, G. The Perdew−Burke−Ernzerhof exchange-correlation functional applied to the G2-1 test set using a plane-wave basis set. *J. Chem. Phys.* **2005**, *122*, 234102.
(32) Grimme, S.; Antony, J.; Ehrlich, S.; Krieg, H. A consistent and accurate ab initio parametrization of density functional dispersion correction (DFT-D) for the 94 elements H-Pu. *J. Chem. Phys.* **2010**, *132*, 154104.
(33) Spiecker, E.; Garbrecht, M.; Jäger, W.; Tillmann, K. Advantages of aberration correction for HRTEM investigation of complex layer compounds. *J. Microsc.* **2010**, *237*, 341−346.
(34) Wiegers, G. A. Misfit layer compounds: Structures and physical properties. *Prog. Solid State Chem.* **1996**, *24*, 1−139.
(35) Lu, J. Y.; Ge, Q.; Raza, A.; Zhang, T. Quantum Mechanical Prediction of Wettability of Multiphase Fluids−Solid Systems at Elevated Temperature. *J. Phys. Chem. C* **2019**, *123*, 12753−12761.
(36) Wan, C.; Wang, Y.; Wang, N.; Koumoto, K. Low-Thermal-Conductivity (MS)1+x(TiS2)2 (M = Pb, Bi, Sn) Misfit Layer Compounds for Bulk Thermoelectric Materials. *Materials* **2010**, *3*, 2606.

https://doi.org/10.1021/acs.jpcc.0c10756
J. Phys. Chem. C 2021, 125, 9956−9964